# Nanodiamonds for spatial resolution benchmarking in two-photon microscopy

Filip Janiak[1,2,$], Michael Forsthofer[1], Jakub Czubek[2], Małgorzata Szczerska[2], Tom Baden[1]

1: Sussex Neuroscience, University of Sussex, Brighton, UK; 2: OpticLab ((Opto and Neuro Laboratory), Faculty of Electronics, Telecommunications and Informatics, Gdansk University of Technology, Gdansk, Poland

[$]Correspondence to f.k.janiak@sussex.ac.uk

**Summary.** Reliable and reproducible measurement of spatial resolution is essential for validating and comparing the performance of two-photon microscopy systems. We present fluorescent nanodiamonds as robust, photostable, reusable, and biocompatible probes for benchmarking spatial resolution. Owing to their nanoscale dimensions and stable fluorescence, nanodiamonds act as near-ideal point-like emitters, enabling accurate characterisation of the point spread function across varying imaging conditions. We demonstrate that nanodiamond-based phantoms serve as a reliable alternative to conventional fluorescent beads embedded in agarose, while at the same time offering advantages in stability and optical properties. Our results position nanodiamond phantoms as a next-generation calibration material that bridges ease of use and reproducibility, advancing quantitative imaging and cross-platform comparability in modern fluorescence microscopy.

---

Acknowledgements: We thank Chrysovalantis Fekos and Miguel Maravall for the mouse brain photo used in Figure 2. Funding was provided by the Wellcome Trust (Investigator Award in Science 220277/Z20/Z), the European Research Council (ERC-StG “NeuroVisEco” 677687 and ERC AdG “Cones4Action” covered under the UK’s EPSRC guarantee scheme EP/Z533981/1), UKRI (BBSRC, BB/R014817/1 and BB/W013509/1), HFSP (RGP001/2025), the Leverhulme Trust (PLP-2017-005, RPG-2021-026 and RPG-2-23-042), the Lister Institute for Preventive Medicine and Gdańsk University of Technology by the DEC-4/1/2024/IDUB/I.1a/No grant under the NOBELIUM and 1/1/2025/IDUB/I.1B/Pt PLATINUM - ‘Excellence Initiative - Research University’ program. To promote Open Access, the authors have applied a CC BY public copyright licence to any Author Accepted Manuscript version arising from this submission. The authors declare no conflict of interest.

**Author contributions:**

| | FJ | MF | JC | MSz | TB |
|---|---|---|---|---|---|
| **Concept** | ■ | | | | |
| **Design** | ■ | | | ■ | |
| **Sample preparation** | | | | ■ | |
| **Data collection** | ■ | ■ | ■ | | |
| **Data Processing** | ■ | ■ | ■ | | |
| **Funding** | ■ | | | | ■ |
| **Writing** | ■ | | | | ■ |

## Introduction

Two-photon scanning microscopy (2PM) is a powerful imaging technique that utilizes simultaneous absorption of two infrared photons to excite fluorophores. This technique reduces out-of-focus excitation and photodamage, making it ideal for imaging thick biological tissues[1]. In neuroscience, 2PM is extensively employed for *in vivo* imaging of neuronal activity, dendritic spines, and synaptic structures, enabling high-resolution visualization within living tissue. The technique has been extensively applied across brain regions and species[2–6].

Accurate spatial resolution measurements ensure that fine structures are correctly and reproducibly visualized. Accordingly, robust methods for spatial-resolution assessment are essential for meaningful within- and cross-platform comparisons[7].

The point spread function (PSF) is a fundamental descriptor of a microscope's spatial resolution[8,9]. It represents the three-dimensional response of the imaging system to a point source, effectively characterizing how light from a single point object spreads in the lateral (x, y) and axial (z) dimensions. This makes the PSF a central metric for validating system performance, optimizing imaging parameters, ensuring reproducibility across experiments, and comparing different two-photon systems.

To accurately measure the PSFs of a multiphoton microscope, researchers typically image sub-resolution fluorescent beads (ideally 100–200 nm in diameter) embedded in low-melting-point agarose gel[7]. A three-dimensional image stack of an isolated bead is acquired with adequate voxel sampling to resolve the PSF. Full width at half maximum (FWHM) measurements are taken along the lateral and axial dimensions to estimate spatial resolution[10]. To identify field-dependent variation or optical distortion, measurements are repeated across multiple regions of the sample. This approach provides a practical baseline for assessing system performance[11]. However, it remains sensitive to preparation inconsistencies and local aberrations, which can introduce variability in the measured PSF[12,13]. Further variability can stem from bead immobilization, sample preparation, and storage conditions[7]. For instance, fluorescent beads are typically embedded in low-melting-point agarose to prevent photobleaching, but improper mixing or cooling before bead incorporation can result in uneven bead distribution, affecting measurements. Additionally, storing the samples at room temperature for extended periods of time can lead to photobleaching or degradation of the beads[14]. In addition, to prevent sample degradation due to evaporation, a glass cover is commonly used, however this glass adds further aberrations.

Here, we use nanodiamond-based samples analogously to conventional fluorescent bead phantoms, i.e. artificial reference samples with controlled optical properties, embedded in agarose for PSF measurements. Beyond their bright and stable two-photon fluorescence[15], nanodiamonds provide key practical advantages for PSF characterization. Their intrinsic nitrogen-vacancy (NV) centre emission does not bleach or chemically degrade, unlike dye-doped beads, and their exceptional chemical stability enables long-term preservation[16]. Consequently, nanodiamond gels maintain their optical and mechanical properties over years; for example, the samples used in this study were prepared in 2018 and showed no observable degradation after long-term storage at room temperature. This long-term robustness allows repeated use of the same phantom across imaging sessions and calibration routines, improving consistency and reducing sample-to-sample variability. Moreover, depending on gel formulation, the refractive index of nanodiamond phantoms can be tuned to approximate that of biological tissues, creating a more physiologically relevant optical environment for benchmarking imaging performance. Together with their excellent biocompatibility[17], these features position nanodiamond-based phantoms as a reliable, reusable, and biologically meaningful standard for high-precision PSF measurements in two-photon microscopy.

## Results

Nanodiamonds are crystalline carbon nanoparticles obtained from controlled high-pressure or detonation synthesis, producing exceptionally stable and biologically compatible materials[17,18]. Many nanodiamonds host (NV) centres that provide bright, highly photostable fluorescence resistant to bleaching[19]. These properties make nanodiamonds attractive as robust, long-term optical probes in demanding biological and materials-science imaging contexts.

### Nanodiamonds as a next-generation calibration material

We used nanodiamond phantoms mimicking physical properties of human tissue in the context of medical imaging (calibrating MRI scans)[20]. The samples were prepared by forming a gel matrix of agar and carrageenan in distilled water. Nanodiamonds were first dispersed in dimethyl sulfoxide (DMSO), a polar aprotic solvent that efficiently wets their surfaces, reduces aggregation, and enables stable mixing with the aqueous gel. Two nanodiamond series were prepared: the *nano* series containing 8–12% (v/v) of a nanodiamonds (ND) standard suspension in DMSO (Adámas Nanotechnologies, 5 nm particles), and the ‘*dnp’* series containing 8–12% (v/v) of the hydrophilic RT-DND-L suspension (Ray Techniques Ltd., 4–5 nm particles). The nanodiamond suspensions were incorporated into the warm gel base, gently heated to ensure homogeneity, and then poured into moulds to solidify into stable phantoms (see Methods for details).

Figure 1a presents scanning electron micrographs (SEM) of an 8% dnp phantom sample. These images reveal a heterogeneous distribution of nanodiamond structures, with a notable fraction measuring under 200 nm, comparable in size to standard fluorescent nanobeads commonly used for PSF calibration. This sub-200 nm population is particularly relevant for imaging-based resolution assessment. The observed size diversity results from the fabrication process, in which individual nanodiamonds, typically 4–5 nm in diameter, form colloidally stable aggregates. Dynamic light scattering confirmed that these aggregates have an average size of approximately 70–80 nm, making them suitable analogues for sub-resolution bead-based calibration[18,20–22].

To support that the fluorescence signal originates from the nanodiamond material rather than added dyes, we acquired confocal z-stacks under 561-nm excitation (Figure 2b). We observed bright, punctate emitters distributed throughout the gel in both formulations, consistent with fluorescent nanodiamond aggregates containing NV centres as reported in the literature[15,23]. This control confirms that the phantoms provide robust intrinsic fluorescence suitable for PSF measurements. Together, these observations support that the fluorescence signal used for PSF measurements originates from the nanodiamond material itself rather than from added dyes, confirming that the phantoms act as a robust, dye-free reference for two-photon imaging and resolution benchmarking.

## Nanodiamond phantoms enable robust and reproducible two-photon PSF measurements

We demonstrate that nanodiamonds give usable PSFs under 2-photon excitation. We compared two-photon PSF measurements (920 nm excitation, 3 mW at the sample, Coherent Vision S femtosecond laser) from one of the nanodiamond samples (8% DNP) with those from a standard fluorescent bead sample (Invitrogen 505/515, P7220) using our two-photon microscopy (2PM) setup. Representative *xz* and *yz* cross-sectional profiles were extracted from *xy* planes of z-stacks acquired sequentially on the same imaging system configured in two modes: diffraction-limited (DL) and an experimentally expanded PSF generated with non-telecentric (nTC) optics[24] (Figure 1c). In both configurations, PSF dimensions were statistically indistinguishable between nanodiamonds and beads (Figure 1d), confirming that nanodiamonds provide reliable, well-defined PSFs suitable for quantitative imaging.

Finally, Figure 1e compares PSF measurements obtained from all six phantom types under identical two-photon microscopy conditions (DL configuration). The analysis confirms consistent optical performance across samples, indicating that the nanodiamond and dynamic nanodiamond polymer phantoms provide reproducible fluorescence characteristics suitable for benchmarking imaging resolution.

## Engineering nanodiamond phantoms to replicate tissue-like imaging conditions

To accurately record the PSF, it is advantageous to match key optical and physical properties that influence image formation. A notable benefit of nanodiamond-based phantoms is that their material properties can be systematically tuned: adjusting nanodiamond concentration, particle size, or surface functionalisation enables controlled modulation of refractive index, scattering coefficient, and fluorescence brightness. Consequently, phantom mixtures can be fabricated to emulate a range of tissue-like conditions, including those found across different brain regions and depths. This tunability ensures that PSF calibration more faithfully reproduces the optical environment of the actual experiment, improving the accuracy and interpretability of downstream imaging measurements.

Figure 2a shows representative photographs of the various samples used in this study: an agarose-bead phantom, the nanodiamond-based phantoms (nano 8% and dnp 8%) and a live adult mouse brain section imaged through a cranial window. The nanodiamond-based phantoms exhibit optical scattering and structural heterogeneity resembling brain tissue more closely than the uniform agarose-bead sample. This visual and optical similarity supports their use as biologically relevant calibration standards.

Figure 2b summarises the refractive indices (RI) of distilled water, 2% agarose gel prepared with water, and six different nanodiamond-based phantom formulations. For comparison, these values are plotted alongside RI estimates of brain tissues from animal models commonly used in 2PM neuroscience experiments: mouse[25–28], rat[27,29], zebrafish[30–34], and fruit flies[35–37]. The RIs of nanodiamonds are approximately in line with estimates from animal brains, most notably from mouse and fruit flies. By contrast, RIs of water and agarose are generally below those of most animal brains.

In addition to the variation in RI across different tissue types, it is important to note that the refractive index measurements were collected at two wavelengths, 589 nm and 1050 nm, which provides insight into the spectral dispersion of the nanodiamond formulations. Comparing RI at these two wavelengths reveals how strongly each formulation's refractive index changes with wavelength: minimal differences indicate low dispersion, whereas larger shifts signal wavelength-dependent optical behaviour that can influence focusing accuracy and aberration levels in two-photon microscopy operating in the near-infrared.

Moreover, the RI-differences observed across nanodiamond samples indicate how responsive the optical properties are to formulation choices. Although effects such as nanodiamond agglomeration[38] likely contribute to the variability seen in the older sample set, these results point to yet unexplored headroom for optimisation. With improved control over dispersion, aggregation, and composition, future nanodiamond-based phantoms can be designed to span a broader and more precisely targeted range of refractive indices that more faithfully reflects the diversity of biological tissues, ultimately enabling even more accurate and customisable PSF calibration.

Overall, our nanodiamond phantoms are designed to mimic the optical behaviour of real tissue rather than the more homogeneous environment of agarose gels. Correspondingly, the PSF should broaden with imaging depth, reflecting the increased scattering and aberrations that also occur in vivo. To assess this depth dependence directly, we measured PSFs in the same nanodiamond sample (nano 10%) at two depths under identical optical conditions. Representative xz and yz sections acquired near the surface (0–50 μm from the top) were compared to data collected approximately 700 μm deeper in the gel (Fig. 2c). Gaussian fitting of lateral and axial intensity profiles yielded full width at half maximum (FWHM) values summarised in Fig. 2d. This directly confirmed that deeper imaging produces broader PSFs, in line with established depth-dependent aberration and scattering effects in biological tissue. These results contrast with agarose-based phantoms, where minimal scattering and refractive-index homogeneity often lead to artificially stable PSFs with depth[7,9,13].

## Nanodiamonds exhibit resistance to PSF saturation and photobleaching

Accurate and reproducible PSF measurements benefit greatly from fluorescent probes that remain stable under a wide range of imaging conditions. Nanodiamonds offer a clear advantage in this context, as their intrinsic NV-centre fluorescence is exceptionally resistant to photobleaching, saturation, and power-dependent nonlinearities[15,23,39,40].

This stability allows PSFs to be recorded reliably even when excitation power, depth, or microscope configuration vary, making nanodiamond-based phantoms particularly well suited for routine calibration and cross-platform benchmarking. By contrast, traditional agarose-embedded fluorescent beads require stringent control of imaging parameters, as their emission can saturate or photobleach under higher excitation powers[7,14], leading to distortions in PSF measurements[41] and reduced reproducibility across microscopes and laboratories[42]. Thus, nanodiamonds provide a more robust and dependable foundation for quantitative optical characterisation.

Figure 3a shows xz images of fluorescent beads and Figure 3b presents corresponding nanodiamond images (bottom, nano 8% sample) acquired under two-photon excitation at increasing power levels. While the bead images clearly saturate at higher excitation powers, the nanodiamonds retain a consistent, well-defined shape across the entire power range. Quantitative analysis based on Gaussian fitting, summarised in Figure 3c, confirms this stability.

These results underscore the exceptional photostability of nanodiamonds: their NV-centre fluorescence exhibits negligible photobleaching and resists saturation even under elevated excitation intensities. Such robustness makes nanodiamonds particularly advantageous for PSF characterisation in realistic imaging conditions, where higher laser powers, deeper imaging, and longer acquisition times are often necessary. Their stable emission and resistance to photodamage provide a reliable and reproducible standard for system calibration in advanced two-photon microscopy setups[40].

### Nanodiamonds support robust imaging across a wide excitation spectrum

Figure 3d shows the XY fluorescence intensity profiles of both beads and nanodiamonds under two-photon excitation across wavelengths from 800 nm to 1040 nm, all acquired at a constant excitation power of 5 mW. The beads, composed of yellow-green fluorescent material (excitation/emission 505/515 nm), remain clearly visible throughout the full excitation range, reflecting their broad two-photon absorption spectrum. The nanodiamonds likewise display consistent fluorescence across all tested wavelengths, demonstrating their robust and efficient two-photon excitation behaviour. This broad excitation responsiveness confirms that both beads and nanodiamonds are compatible with multi-wavelength imaging modalities, while further emphasising the versatility of nanodiamonds as stable and reliable contrast agents in a wide range of two-photon microscopy conditions.

## Discussion

Quantitative and reproducible assessment of spatial resolution remains a central challenge in two-photon microscopy. Existing calibration samples such as fluorescent beads embedded in agarose are limited by photobleaching, mechanical instability, and optical properties that differ markedly from those of biological tissue. Here we show that fluorescent nanodiamond phantoms overcome these constraints and establish a new class of calibration standard for PSF characterisation. The intrinsic nitrogen vacancy fluorescence of NDs is exceptionally stable, resisting saturation and photobleaching even under elevated excitation powers. As a result, ND phantoms deliver PSF measurements that remain unchanged across repeated imaging sessions, long-term storage, and variations in acquisition conditions.

A defining strength of the ND formulation is its close optical correspondence to mammalian brain tissue. By matching refractive index and reproducing the subtle scattering and aberrations encountered in vivo, ND gels capture the depth-dependent degradation of axial resolution observed during real biological imaging. This behaviour bridges the gap between idealised calibration samples and the complex optical environments encountered in practical microscopy. Importantly, the depth-dependent PSF broadening measured in ND samples mirrors in vivo performance and enables predictive calibration. Users can therefore anticipate the performance of their imaging system at depth and optimise optical correction strategies before undertaking live experiments.

The stability and reproducibility of ND phantoms extend their impact beyond calibration of individual instruments. Because a single batch can be distributed across laboratories without measurable optical drift, ND phantoms provide a realistic foundation for cross-platform and multi-centre benchmarking. This capability addresses a major gap in advanced fluorescence microscopy and supports the development of shared reference datasets, longitudinal performance tracking, and harmonised quality-assurance protocols similar to those used in clinical imaging.

The tissue-like optical behaviour of ND phantoms arises from nanoscale heterogeneity that is intrinsic to the material. Nanodiamond aggregates in the sub-200 nanometre range create scattering microenvironments that approximate neural tissue far more closely than homogeneous gels. This results in PSFs that are slightly broader than those produced by ideal bead standards but that more accurately represent conditions encountered in biological samples. ND phantoms therefore provide an effective testbed for evaluating new optical designs, adaptive optics methods, and deep-imaging strategies under conditions that reflect realistic imaging challenges.

Equally important is the practical accessibility of this approach. ND phantoms are inexpensive, relatively straightforward to fabricate, stable at room temperature, and compatible with standard sample holders and immersion media. Their durability removes the need for frequent sample preparation or controlled storage, which reduces operational variability and enables routine calibration in both academic and industrial microscopy facilities.

Taken together, these properties position nanodiamond phantoms as a useful advance in two-photon microscopy calibration. Their combination of long-term fluorescence stability, tissue-relevant optical characteristics, and resistance to power-related artefacts extends accurate resolution benchmarking into regimes that were previously inaccessible with conventional reference materials. Further refinement of their optical tuning through controlled adjustment of aggregate size, refractive index, or scattering coefficient could yield phantoms tailored to specific tissues and imaging depths. Broad adoption of such physiologically relevant calibration materials has the potential to improve reproducibility, comparability, and methodological transparency across the fluorescence microscopy community and to accelerate progress in both fundamental neuroscience and biomedical imaging technology.

## Methods

### *RI measurements*

The refractive index at 589 nm and 1050 nm was measured using an Atago Multi-Wavelength Abbe Refractometer (model DR-M2). To maintain uniformity and reduce thermal variability in the RI values, all measurements were carried out at a regulated temperature of 22 °C.

### *Mouse brain photo*

The photo presents part of the adult mouse brain (C57BL/6J genetic background) taken through a cranial window at the University of Sussex. The photos of the agarose sample and phantoms has been taken by the same camera in the same illumination conditions. A circular craniotomy (3 mm diameter; coordinates from bregma: 1mm caudal, 3mm to the right) was performed to allow for accessing the barrel cortex (whisker-related area of the primary somatosensory cortex (wS1) in mice).

### *Scanning Electron Microscopy images*

SEM imaging was carried out using an SM-7800F Schottky Field Emission Scanning Electron Microscope (JEOL Ltd., Japan). Multiple magnifications were applied to capture both micro- and nanoscale features of the samples. electron beam and image quality. A low-voltage electron source (1.00 kV) was used to prevent surface melting of the agar–carrageenan matrix observed at higher beam energies. Acquired images were post-processed using ImageJ software (version 1.54g) in combination with the DeconvolutionLab2 plugin (version 2.1.2). The Richardson–Lucy deconvolution algorithm was applied with 10 iterations to enhance image clarity and contrast.

### *Two – photon setup*

The excitation beam was generated using a tuneable femtosecond Ti:Sapphire laser (Coherent Vision-S, 75 fs, 80 MHz, >2.5 W). The beam passed through an achromatic half-wave plate (AHWP05M-980, Thorlabs) and was split equally into two independent two-photon (2P) setups using a beam-splitter (10RQ00UB.4, Newport). It then passed through a Pockels cell (350-80, Conoptics), a telescope (AC254-075-B and AC254-150-B, Thorlabs), and was reflected by three silver mirrors (PF10-03-P01) into the head of a Sutter MOM stage. The beam was directed using galvanometric mirrors (6215H, Cambridge Technology). In diffraction diffraction-limited configuration, it was focused into a 50 mm focal length scan lens (VISIR 1534SPR136, Leica) and further collimated by a 200 mm focal length tube lens (MXA22018, Nikon). In the Non-Collimated configuration ($nTC_1$), the scan lens was modified to shift its focal length to 190 mm, and an additional plano-convex lens (175 mm) was added. The beam was reflected by two silver parabolic mirrors and passed through a dichroic mirror (T470/640rpc, Chroma) before slightly overfilling the back aperture of a Zeiss Objective W “Plan-Apochromat” ×20/1.0 to create a diffraction-limited excitation spot at a working distance of 1.8 mm. Fluorescence light was collected exclusively through the objective. A dichroic mirror (T470/640rpc, Chroma) reflected the fluorescence into a 140 mm focal length collecting lens, followed by a 580-nm dichroic mirror (H 568 LPXR, superflat). The signal was split into green and red channels using bandpass filters (ET525/50 and ET605/50, Chroma) and focused onto PMT detectors (H10770PA-40, Hamamatsu) using an aspheric condenser lens (G317703000, Linos). Image was acquired by custom-written software (ScanM) controlled the setup via IGOR Pro 6.3 (Wavemetrics). Laser blanking occurred during the turnarounds using the Pockels cell,

### *Fabrication of agarose-based sample with beads*

We utilized 0.175 ± 0.005 µm yellow-green (505/515) fluorescent beads (P7220, Invitrogen) for the calibration and imaging experiments. These beads were specifically chosen for their consistent size and well-characterized fluorescent properties, which are ideal for evaluating the resolution and point spread function (PSF) of the optical system. To prepare the calibration samples, the beads were carefully embedded within a block of low melting point agarose (Fisher Scientific, BP1360-100) at a depth of 1 mm. The agarose concentration was precisely adjusted to 0.75%, ensuring an optimal balance between sufficient rigidity for immobilizing the beads and minimal optical scattering to maintain clarity during imaging. This arrangement provided a stable and reproducible medium that allowed for accurate imaging and quantification of the optical properties, making it a reliable calibration standard for the two-photon microscopy setup

### *Fabrication of nanodiamonds phantoms*

Nanodiamond-based phantoms were fabricated to provide long-term stable and biologically relevant calibration materials for quantitative resolution benchmarking in two-photon microscopy, particularly for applications requiring tissue-mimicking optical properties. All phantoms were prepared using a standardized gel base composed of 1.413 g agar and 2.0 g carrageenan dissolved in 100 mL of distilled water. This mixture was heated until fully homogenized, ensuring complete dissolution of the polysaccharides and the formation of a consistent, mechanically stable gel network. Two families of nanodiamond formulations were incorporated into this matrix. The nano series consisted of 8–12% (v/v) of an ND-Standard suspension in dimethyl sulfoxide (DMSO) supplied by Adámas Nanotechnologies, containing 5 nm particles with well-characterized NV fluorescence. The dnp series used corresponding concentrations (8–12% v/v) of an RT-DND-L hydrophilic nanodiamond suspension from Ray Techniques Ltd., made by dispersing nanodiamond powder at 0.1% (w/w) into DMSO to create a uniform, optically stable stock solution of 4–5 nm particles. After the gel base cooled to room temperature, the DMSO-based nanodiamond suspensions were added and thoroughly mixed to achieve uniform nanoparticle distribution throughout the gel. The mixtures were poured into custom-designed molds and allowed to solidify, producing phantoms with reproducible geometry and consistent optical behaviour. All samples were processed under identical thermal and sterilization conditions, which ensured stable incorporation of nanodiamonds into the gel matrix and prevented microbial contamination during long-term storage. These phantoms were originally fabricated in 2018 as part of a broader effort to develop tissue-mimicking materials for MRI calibration and optical imaging research[43,44]. Remarkably, the same samples were used for the experiments reported here in 2025, and they retained their structural integrity, fluorescence brightness, and nanoparticle dispersion over seven years. Their long-term stability highlights the robustness of the nanodiamond–DMSO–gel formulation and confirms its suitability for reproducible PSF characterisation, cross-instrument comparison, and routine calibration tasks in advanced microscopy workflows.

### ***Confocal images***

Confocal images of samples were taken on a Leica TCS SP8 inverted microscope, using a HC PL APO 63x/1.20 water objective. ~500 micron thick samples were coverslipped in aqua-poly/mount (Polysciences, 18606) and imaged with the 561 nm (69% laser power) laser line. Image stacks of 50x50x50 µm were acquired at a pixel size of 0.1 x 0.1 x 0.36 µm (x, y, z) and visualized as a 3d volume using napari. Fluorescence was collected using a broad detection window to maximize signal-to-noise in thick samples; no spectral unmixing or charge-state discrimination was performed.

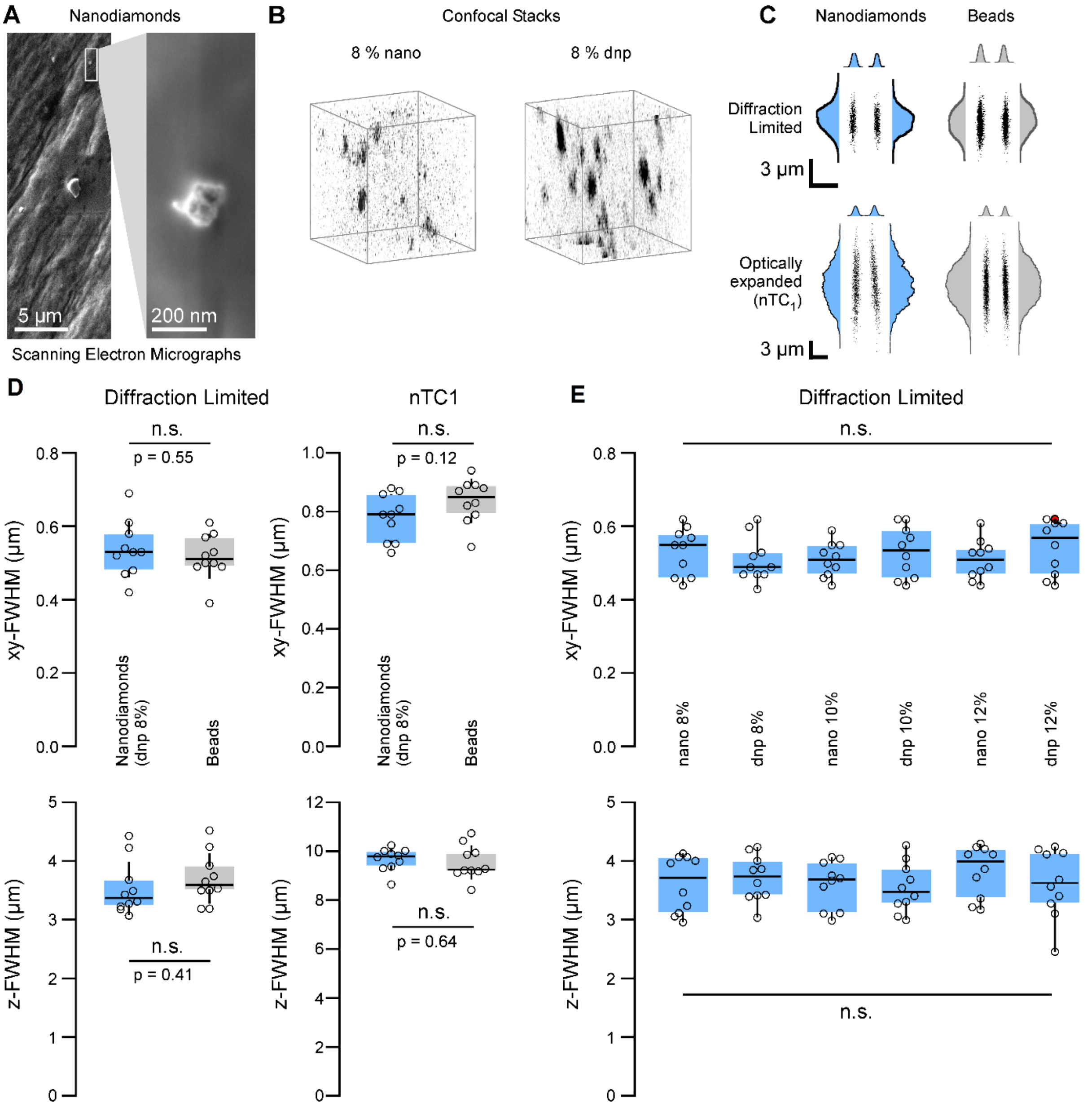

Figure 1. **Structural characterisation and two-photon PSF measurements of nanodiamond-based phantoms.**

(a) Scanning electron microscopy (SEM) images of an 8% dnp nanodiamond phantom reveal heterogeneous nanodiamond aggregates with a substantial fraction below 200 nm, comparable in size to standard fluorescent beads used for PSF calibration.

(b) Volumetric confocal microscopy of nano 8% and dnp 8% phantoms acquired under 561-nm excitation shows bright punctate emitters distributed throughout the gel, consistent with fluorescent nanodiamond aggregates hosting NV centres (literature). These data support that the fluorescence is intrinsic to the nanodiamond material and suitable for use as a dye-free reference.

(c) Representative xz and yz cross-sections of two-photon PSFs recorded from nanodiamonds (8% DNP) and commercial fluorescent beads (Invitrogen 505/515) under diffraction-limited (DL) and non-telecentric (nTC) imaging configurations. All PSFs were acquired using 920 nm excitation at 3 mW on the same two-photon system.

(d) Quantitative PSF analysis shows statistically indistinguishable lateral and axial FWHM values between nanodiamonds and beads in both DL and nTC modes, demonstrating that nanodiamonds provide accurate, bead-equivalent PSFs suitable for microscope performance evaluation.

(e) PSF measurements obtained from all six nanodiamond and dynamic nanodiamond polymer phantoms (DL configuration) exhibit consistent optical performance across formulations, confirming their reproducibility and suitability as robust fluorescence standards for two-photon imaging.

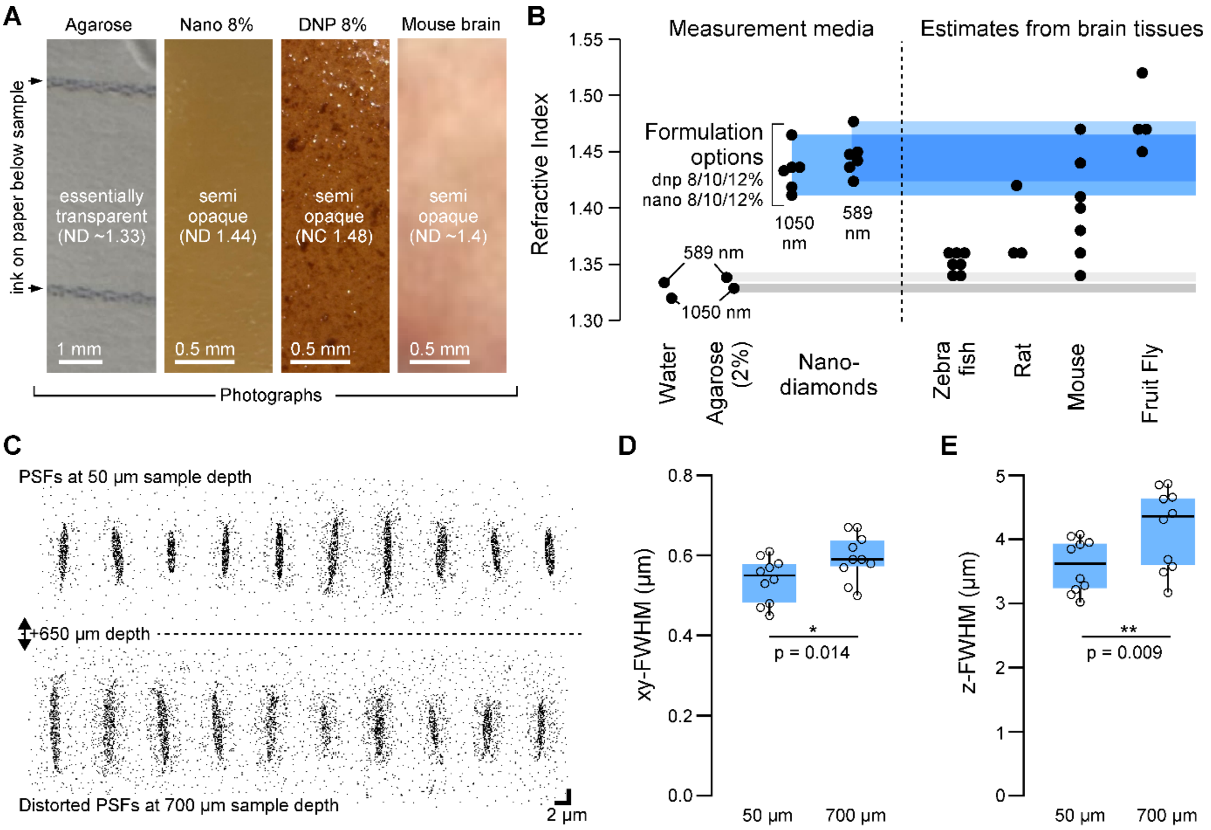

Figure 2. **Optical properties, tissue relevance, and depth-dependent PSF performance of nanodiamond phantoms.**

(a) Representative images of the different phantom types: agarose-bead, nanodiamond (nano %, dnp 8%), and a live adult mouse brain section, acquired under two-photon microscopy. Nanodiamond phantoms exhibit optical scattering and structural heterogeneity that more closely resemble brain tissue than homogeneous agarose gels.

(b) Refractive indices (RI) of distilled water, agarose gel, and six nanodiamond-based formulations measured at 589 nm and 1050 nm, compared with RI estimates from commonly used neuroscience model organisms (mouse, rat, zebrafish, drosophila). Nanodiamond phantoms align more closely with the RI range of biological tissues than agarose, supporting their relevance for realistic PSF calibration.

(c) Two-photon PSFs recorded in a nano 10% phantom at shallow (0–50 µm) and deep (~700 µm) imaging depths under identical optical conditions. Representative xz/yz sections illustrate depth-dependent broadening due to increased scattering and aberrations.

(d) Lateral (x–y) and axial (z) FWHM values derived from Gaussian fits show significant PSF degradation with depth (one-way ANOVA, $p < 0.05$), closely matching depth-dependent resolution loss in vivo. This behaviour contrasts with agarose phantoms, which yield artificially stable PSFs due to minimal scattering.

(e) Conceptual summary: nanodiamond phantoms capture physiologically realistic PSF degradation because their scattering, refractive index, and NV-based fluorescence more accurately model brain tissue. Their tunable composition enables controlled modulation of optical properties for targeted calibration across a wide range of imaging conditions.

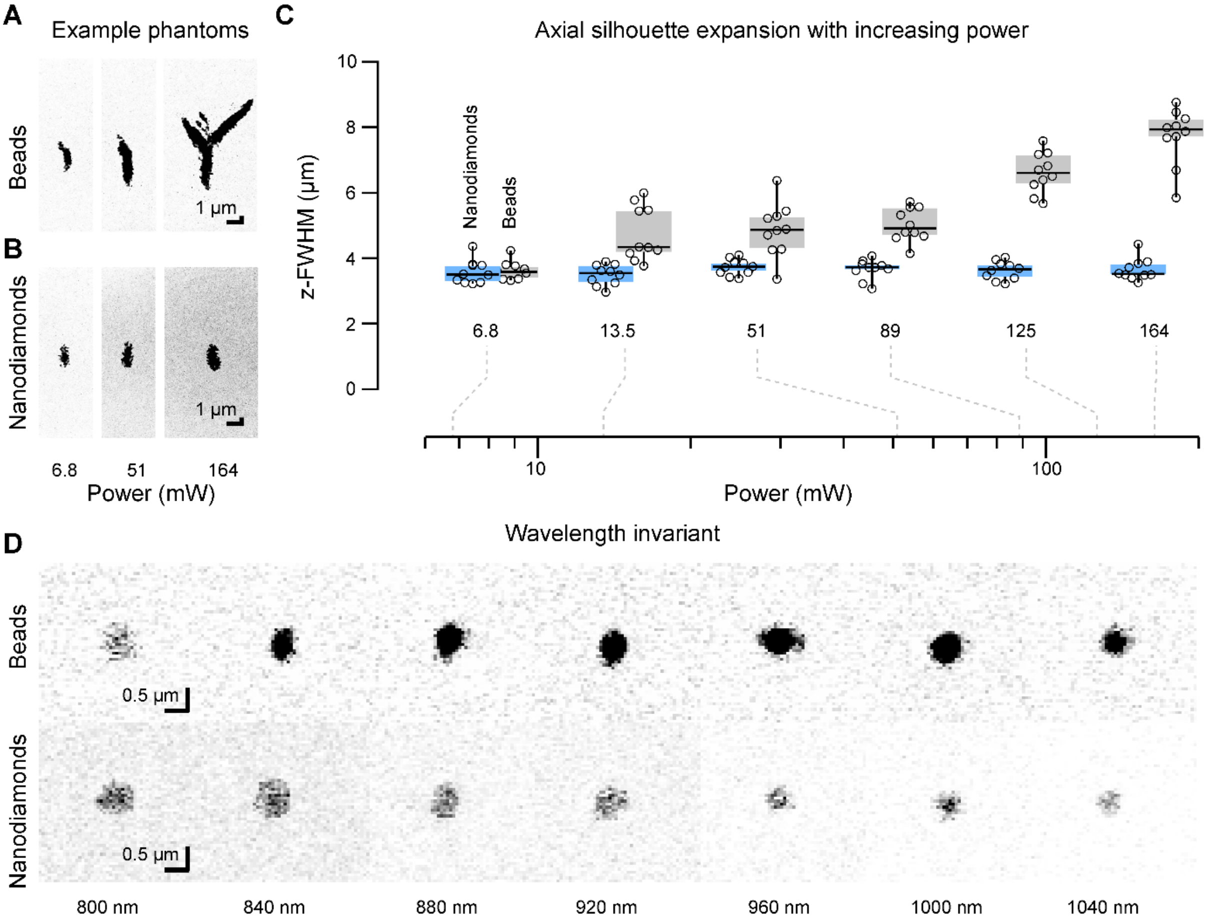

Figure 3. **Photostability and excitation-wavelength robustness of nanodiamonds under two-photon imaging.**
(a) XZ images of commercial fluorescent beads acquired at increasing two-photon excitation powers. Beads exhibit clear saturation and shape distortion at higher power.
(b) Corresponding xz images of nanodiamonds (nano 8% sample) showing well-preserved morphology across the same excitation power range, indicating exceptional resistance to saturation and photobleaching.
(c) Gaussian fits of lateral and axial profiles extracted from (a–b). Nanodiamonds maintain consistent FWHM values across all excitation intensities, whereas beads show power-dependent broadening and saturation-related deviations.
(d) XY fluorescence intensity profiles of beads and nanodiamonds under two-photon excitation from 800 nm to 1040 nm at a constant power of 5 mW. Beads (excitation/emission 505/515 nm) remain bright across the range, reflecting their broad two-photon absorption spectrum. Nanodiamonds likewise exhibit stable NV-centre fluorescence at all wavelengths tested, confirming efficient and broadband two-photon excitation.

## References:

1. Denk, W., Strickler, J. H. & Webb, W. W. Two-Photon Laser Scanning Fluorescence Microscopy. *Science* **248**, 73–76 (1990).
2. Svoboda, K. & Yasuda, R. Principles of Two-Photon Excitation Microscopy and Its Applications to Neuroscience. *Neuron* **50**, 823–839 (2006).
3. Zhou, M. *et al.* Zebrafish Retinal Ganglion Cells Asymmetrically Encode Spectral and Temporal Information across Visual Space. *Curr. Biol.* **30**, 2927-2942.e7 (2020).
4. Bando, Y., Wenzel, M. & Yuste, R. Simultaneous two-photon imaging of action potentials and subthreshold inputs in vivo. *Nat. Commun.* **12**, 7229 (2021).
5. Dunn, T. W. *et al.* Neural Circuits Underlying Visually Evoked Escapes in Larval Zebrafish. *Neuron* **89**, 613–628 (2016).
6. Ebina, T. *et al.* Two-photon imaging of neuronal activity in motor cortex of marmosets during upper-limb movement tasks. *Nat. Commun.* **9**, 1879 (2018).
7. Lees, R. M. *et al.* Standardized measurements for monitoring and comparing multiphoton microscope systems. *Nat. Protoc.* 1–38 (2025) doi:10.1038/s41596-024-01120-w.
8. Mondal, P. P. & Diaspro, A. Chapter Four - Point Spread Function Engineering for Super-Resolution Single-Photon and Multiphoton Fluorescence Microscopy. in *Advances in Imaging and Electron Physics* (ed. Hawkes, P. W.) vol. 175 201–219 (Elsevier, 2013).
9. Dong, C.-Y., Koenig, K. & So, P. Characterizing point spread functions of two-photon fluorescence microscopy in turbid medium. *J. Biomed. Opt.* **8**, 450 (2003).

10. Cole, R. W., Jinadasa, T. & Brown, C. M. Measuring and interpreting point spread functions to determine confocal microscope resolution and ensure quality control. *Nat. Protoc.* **6**, 1929–1941 (2011).
11. Sofroniew, N. J., Flickinger, D., King, J. & Svoboda, K. A large field of view two-photon mesoscope with subcellular resolution for in vivo imaging. *eLife* **5**, e14472 (2016).
12. North, A. J. Seeing is believing? A beginners’ guide to practical pitfalls in image acquisition. *J. Cell Biol.* **172**, 9–18 (2006).
13. Egner, A. & Hell, S. W. Aberrations in Confocal and Multi-Photon Fluorescence Microscopy Induced by Refractive Index Mismatch. in *Handbook Of Biological Confocal Microscopy* (ed. Pawley, J. B.) 404–413 (Springer US, Boston, MA, 2006). doi:10.1007/978-0-387-45524-2_20.
14. Confocal and Two-Photon Microscopy: Foundations, Applications and Advances | Wiley. *Wiley.com* https://www.wiley.com/en-us/Confocal+and+Two-Photon+Microscopy%3A+Foundations%2C+Applications+and+Advances-p-9780471409205.
15. Tisler, J. *et al.* Fluorescence and Spin Properties of Defects in Single Digit Nanodiamonds. *ACS Nano* **3**, 1959–1965 (2009).
16. Vaijayanthimala, V. *et al.* The long-term stability and biocompatibility of fluorescent nanodiamond as an *in vivo* contrast agent. *Biomaterials* **33**, 7794–7802 (2012).
17. Chauhan, S., Jain, N. & Nagaich, U. Nanodiamonds with powerful ability for drug delivery and biomedical applications: Recent updates on in vivo study and patents. *J. Pharm. Anal.* **10**, 1–12 (2020).

18. Mochalin, V. N., Shenderova, O., Ho, D. & Gogotsi, Y. The properties and applications of nanodiamonds. *Nat. Nanotechnol.* **7**, 11–23 (2012).
19. Alkahtani, M. H. *et al.* Fluorescent nanodiamonds: past, present, and future. *Nanophotonics* **7**, 1423–1453 (2018).
20. Sękowska, A. *et al.* Nanodiamond phantoms mimicking human liver: perspective to calibration of T1 relaxation time in magnetic resonance imaging. *Sci. Rep.* **10**, 6446 (2020).
21. Shenderova, O., Hens, S. & McGuire, G. Seeding slurries based on detonation nanodiamond in DMSO. *Diam. Relat. Mater.* **19**, 260–267 (2010).
22. Krueger, A. & Lang, D. Functionality is Key: Recent Progress in the Surface Modification of Nanodiamond. *Adv. Funct. Mater.* **22**, 890–906 (2012).
23. Bradac, C. *et al.* Observation and control of blinking nitrogen-vacancy centres in discrete nanodiamonds. *Nat. Nanotechnol.* **5**, 345–349 (2010).
24. Janiak, F. K. *et al.* Non-telecentric two-photon microscopy for 3D random access mesoscale imaging. *Nat. Commun.* **13**, 544 (2022).
25. Abookasis, D. & Meitav, O. Assessing mouse brain tissue refractive index in the NIR spectral range utilizing spatial frequency domain imaging technique combined with processing algorithms. in vol. 10864 108640R (2019).
26. Lee, A. J. *et al.* Volumetric Refractive Index Measurement and Quantitative Density Analysis of Mouse Brain Tissue with Sub-Micrometer Spatial Resolution. *Adv. Photonics Res.* **4**, 2300112 (2023).
27. Binding, J. *et al.* Brain refractive index measured in vivo with high-NA defocus-corrected full-field OCT and consequences for two-photon microscopy. *Opt. Express* **19**, 4833–4847 (2011).

28. Ryu, Y. *et al.* Single-Step Fast Tissue Clearing of Thick Mouse Brain Tissue for Multi-Dimensional High-Resolution Imaging. *Int. J. Mol. Sci.* **23**, 6826 (2022).

29. Sun, J., Lee, S. J., Wu, L., Sarntinoranont, M. & Xie, H. Refractive index measurement of acute rat brain tissue slices using optical coherence tomography. *Opt. Express* **20**, 1084–1095 (2012).

30. Schlüßler, R. *et al.* Mechanical Mapping of Spinal Cord Growth and Repair in Living Zebrafish Larvae by Brillouin Imaging. *Biophys. J.* **115**, 911–923 (2018).

31. Boothe, T. *et al.* A tunable refractive index matching medium for live imaging cells, tissues and model organisms. *eLife* https://elifesciences.org/articles/27240 (2017) doi:10.7554/eLife.27240.

32. Philipp, K. *et al.* Diffraction-limited axial scanning in thick biological tissue with an aberration-correcting adaptive lens. *Sci. Rep.* **9**, 9532 (2019).

33. Horst, J. van der, Trull, A. K. & Kalkman, J. Deep-tissue label-free quantitative optical tomography. *Optica* **7**, 1682–1689 (2020).

34. Favre-Bulle, I. A. *et al.* Scattering of Sculpted Light in Intact Brain Tissue, with implications for Optogenetics. *Sci. Rep.* **5**, 11501 (2015).

35. Pende, M. *et al.* High-resolution ultramicroscopy of the developing and adult nervous system in optically cleared Drosophila melanogaster. *Nat. Commun.* **9**, 4731 (2018).

36. Bekkouche, B. M. B., Fritz, H. K. M., Rigosi, E. & O'Carroll, D. C. Comparison of Transparency and Shrinkage During Clearing of Insect Brains Using Media With Tunable Refractive Index. *Front. Neuroanat.* **14**, (2020).

37. Ke, M.-T. *et al.* Super-Resolution Mapping of Neuronal Circuitry With an Index-Optimized Clearing Agent. *Cell Rep.* **14**, 2718–2732 (2016).

38. Voitylov, A. V. *et al.* Light refraction in aqueous suspensions of diamond particles. *Colloids Surf. Physicochem. Eng. Asp.* **538**, 417–422 (2018).
39. Alkahtani, M. H. *et al.* Fluorescent nanodiamonds: past, present, and future. *Nanophotonics* **7**, 1423–1453 (2018).
40. Faklaris, O. *et al.* Detection of Single Photoluminescent Diamond Nanoparticles in Cells and Study of the Internalization Pathway. *Small* **4**, 2236–2239 (2008).
41. Zipfel, W. R., Williams, R. M. & Webb, W. W. Nonlinear magic: multiphoton microscopy in the biosciences. *Nat. Biotechnol.* **21**, 1369–1377 (2003).
42. Juškaitis, R. Measuring the Real Point Spread Function of High Numerical Aperture Microscope Objective Lenses. in *Handbook Of Biological Confocal Microscopy* (ed. Pawley, J. B.) 239–250 (Springer US, Boston, MA, 2006). doi:10.1007/978-0-387-45524-2_11.
43. Wróbel, M. S. *et al.* Model of optical phantoms thermal response upon irradiation with 975 nm dermatological laser. in *Saratov Fall Meeting 2017: Optical Technologies in Biophysics and Medicine XIX* vol. 10716 13–18 (SPIE, 2018).
44. Listewnik, P., Ronowska, M., Wąsowicz, M., Tuchin, V. V. & Szczerska, M. Porous Phantoms Mimicking Tissues—Investigation of Optical Parameters Stability Over Time. *Materials* **14**, 423 (2021).